Supplementary Information

An Electric Double-layer Capacitor with High Performance at −80 ˚C

Haofeng Liu,[ag] Feng Zhou,*[a] Zekai Zhang,[c] Haodong Wang,[a] Hanqing Liu,[d] Zhihao Ren,[ag] Endian Yang,[a] Zhengdong Ma,[ae] Tongle Chen,[a] Pratteek Das,[a] Changde Ma,[a] Ao Leng,[a] Shihao Liao,[a] Xiong Zhang,[f] Yabin An,[f] Cheng Lian,[c] Yanwei Ma,[f] Hui-Ming Cheng,*[bhij] and Zhong-Shuai Wu*[adg]

[a]State Key Laboratory of Catalysis, Dalian Institute of Chemical Physics, Chinese Academy of Sciences, Dalian, China. E-mail: zhoufeng1107@dicp.ac.cn; wuzs@dicp.ac.cn

[b]Shenzhen Key Lab of Energy Materials for Carbon Neutrality, Shenzhen Institutes of Advanced Technology, Chinese Academy of Sciences, 1068 Xueyuan Road, Shenzhen, China. E-mail: hm.cheng@siat.ac.cn

[c]School of Chemical and Molecular Engineering, East China University of Science and Technology, Shanghai, China.

[d]Dalian National Laboratory for Clean Energy, Chinese Academy of Sciences, Dalian, China.

[e]Institute of Advanced Electrochemical Energy, School of Materials Science and Engineering, Xi'an University of Technology, Xi'an, China.

[f]Institute of Electrical Engineering, Chinese Academy of Sciences, Beijing, China.

[g]University of Chinese Academy of Sciences, Beijing, China.

[h]Faculty of Materials Science and Energy Engineering, Shenzhen University of Advanced Technology, 291 Louming Road, Shenzhen, China.

[i]Shenyang National Laboratory for Materials Science, Institute of Metal Research, Chinese Academy of Sciences, 72 Wenhua Road, Shenyang, China.

[j]SKKU Global Center, Sungkyunkwan University, Suwon, Republic of Korea.

This file includes:

Methods

Materials and EDLCs assembly

The ionic liquid N-methoxyethyl-N-methylpyrrolidinium bis(trifluoromethanesulfonyl)imide ($P_{1,2O1}$TFSI) was purchased from the Lanzhou Institute of Chemical Physics, acetonitrile (ACN) from DoDochem, and 1,1,2,2-tetrafluoroethyl 2,2,2-trifluoroethyl ether (HFE-347) from Macklin. All the electrolytes were prepared in an argon-filled glove box maintaining O_2 and H_2O levels below 0.01 ppm. The electrolyte used in this study was prepared by mixing $P_{1,2O1}$TFSI, ACN and HFE-347 at mass ratios of 4:2:4 (PAH), while the electrolytes for comparison were prepared by mixing $P_{1,2O1}$TFSI with ACN at 4:6 (PA-1) and with HFE-347 at 4:6 (PH-1) mass ratios. The electrolytes for solvation structures analysis were prepared by mixing $P_{1,2O1}$TFSI and ACN with a mass ratio of 2:1 (PA-2), and $P_{1,2O1}$TFSI and HFE-347 with a mass ratio of 1:1 (PH-2).

The activated carbon (YP80F) was purchased from Kuraray, and potassium hydroxide (KOH) was purchased from Macklin. The activated carbon (AC) was mixed with KOH in a mass ratio of 8:1 (KOH to YP80F) and heated in an argon atmosphere to 900 °C at a rate of 10 °C min^{-1}, where it remained for 2 hours to create mesopores. After etching, the sample was cooled to room temperature at a rate of 10 °C min^{-1} and washed with dilute hydrochloric acid (36.5 wt%) to reach a neutral pH, and then repeatedly washed with deionized water by vacuum filtration before drying at 100 °C in a vacuum.

Electrodes were coated on a carbon-coated aluminum foil with mass loading of about 1.5 mg cm^{-2} with a composition of 80 wt% active material, 10 wt% conductive carbon black, 5 wt% carboxymethyl cellulose and 5 wt% styrene butadiene rubber. CR2016 coin-type EDLCs were assembled with glass fiber separator (GF-A) between two electrodes and 100 µL electrolyte was injected into the cell before it was encapsulated. For pouch-type EDLCs, a cellulose separator (TF4030) was used, and etched aluminum foil served as the current collector. The mass loading of active material for the pouch-type EDLC electrodes was approximately 5 mg cm^{-2}. All the EDLCs were assembled in an argon-filled glove box with O_2 and H_2O levels maintained below 0.01 ppm.

Electrochemical measurements

The electrochemical stability window (ESW) of the PAH electrolyte was evaluated by linear sweep voltammetry (LSV), using glassy carbon as the working electrode, a platinum sheet as the counter electrode, and a silver wire as the quasi-reference electrode. The ionic conductivities (σ) of the electrolytes were measured at different temperatures using electrochemical impedance spectroscopy (EIS) at frequencies of 0.01 Hz to 100 kHz with an AC amplitude of 5 mV. The tests were conducted using CR2016 cells configured as stainless steel | electrolyte | stainless steel. The ionic conductivities were calculated using the following equation[1]:

$$\sigma = \frac{L}{R_S A}$$

where L is the thickness of the electrolytes (the distance between the two stainless steel electrodes), R_S is the electrolyte resistances from EIS, and A is the geometric area

of the electrode. The electrochemical performance was tested using an electrochemical workstation (CHI 760E), Wuhan Land Battery Testing System and NEWARE Battery Testing System. At low temperatures, the device was first placed in a low-temperature chamber for 2 hours to stabilize the temperature before testing. The low-temperature chamber has a fluctuation of ±2 °C during the temperature-holding process. The specific capacitance (F g^{-1}) of the electrode was calculated using the following formula:

$$C_E = \frac{I * \Delta t}{m \Delta V} * 4$$

where *I* is the current during the GCD measurements, *Δt* is the discharge time (s), Δ*V* is the discharge voltage window after removing the ohmic drop, and *m* is the total mass of the active material of the two electrodes. The energy density (*E*, Wh kg^{-1}) and power density (*P*, W kg^{-1}) of supercapacitors were calculated using the following formulae:

$$E = \frac{0.5 * C * \Delta V^2}{3.6}$$

$$P = \frac{E * 3600}{\Delta t}$$

where *C* (F g^{-1}) is one fourth of C_E, ΔV is the discharge voltage window after removing the ohmic drop, and Δt is the discharge time (s).

The ionic diffusion coefficients were calculated from the EIS spectra in the low-frequency region using the following equation[2]:

$$D = \frac{R^2 T^2}{2 A^2 n^4 F^4 C^2 \sigma^2}$$

where σ is the Warburg coefficient obtained from the slope of the Z' *vs.* $\omega^{-1/2}$ plot, R is the gas constant, T is the temperature, A is the electrode area, n is the number of electrons transferred, which is equal to 1, F is the Faraday constant, and C is the ionic concentration of the electrolyte.

Characterizations

The phase change temperature of the electrolytes was characterized using a differential scanning calorimeter (DSC 204 HP, NETZSCH) over the temperature range −100 °C to 10 °C at a rate of 5 °C·min^{-1} under a nitrogen atmosphere. Fourier transform infrared spectroscopy with attenuated total reflection (FTIR-ATR) tests were conducted on an INVENIO S (Bruker) instrument. XRD tests were performed in SmartLab SE, Rigaku, with Cu K_α of wavelength 1.542 Å. Room-temperature Raman spectroscopy tests were done using a Bruker Optics Senterra with a 532 nm excitation laser. For variable-temperature Raman spectroscopy, an HNG-ISRaman instrument was used with a 352 nm excitation laser. Nuclear magnetic resonance (NMR) spectra were recorded on a JNM-ECZL400S spectrometer (400 MHz) using a coaxial NMR tube. The inner tube contained the test samples, while the outer tube was filled with deuterated chloroform as the deuterium solvent and tetramethylsilane (TMS) as the internal standard at room temperature. For low-temperature measurements, deuterated acetone replaced deuterated chloroform in the outer tube. The morphological and structural characterizations of samples were examined using transmission electron microscopy (TEM, JEM 2100, Japan). Nitrogen adsorption-desorption isotherm measurements were examined using ASAP 2020 and Quadrasorb

evo instruments. X-ray photoelectron spectroscopy (XPS) measurements were performed using an ESCALAB250xi instrument. Contact angle measurements were conducted using a DSA100 instrument. Scanning electron microscopy (SEM) measurements were performed on an S5500 instrument.

Computational methods

All electronic structures in this work were fully optimized using the Gaussian 09 suite of the program by the B3LYP /6-311+G (d, p), including the empirical dispersion corrections BSSE method, and were performed using the tight convergence criterion, which was always followed by the calculation of harmonic vibrational modes.[3–6] Based on the optimized molecular structures, the energy level was analyzed by the Multiwfn program and visualized using the VMD package according to the molecular frontier orbital theory.[7,8] All basis sets were obtained from the Basis Set Exchange library.

We used Gromacs package for MD simulations, and the force field parameters were based on OPLS-AA.[9,10] The nanochannel was formed by carbon nanotube and the diameter of nanochannel was controlled by changing the chirality of carbon nanotube The diameters of nanochannels were 2.29 nm and 3.36 nm, which were respectively related to carbon nanotubes with chiralities of (17,17) and (25,25). The length of a nanochannel was 5 nm. The nanochannel was frozen throughout the simulations. The simulations were conducted in a NVT ensemble for 10 ns with a time step of 1 fs. The temperature was controlled at 298.15 K. The long-range electrostatic interactions were handled by the particle-mesh Ewald (PME) method with a cutoff radius of 1.4 nm. The LINCS algorithm constrains the bonds containing hydrogen

atoms.[11,12] The Verlet algorithm was used as an integrator of Newton's equation of motion.[13]

The diffusion coefficients (*D*) were computed from the corresponding mean-square displacement (MSD) according to the following equation:

$$D = \lim_{t\to\infty} D^{app}(t) = \lim_{t\to\infty} \frac{\langle MSD(t)\rangle}{6t} = \lim_{t\to\infty} \frac{d}{6t}\left\langle \sum_{\alpha} \left[r_i^{\alpha}(t) - r_i^{\alpha}(0)\right]^2 \right\rangle$$

where $r_i^{\alpha}(t)$ is the position of atom *i* of type *α* at time *t*. The brackets denote an ensemble average over all trajectories and atoms *i* of type.

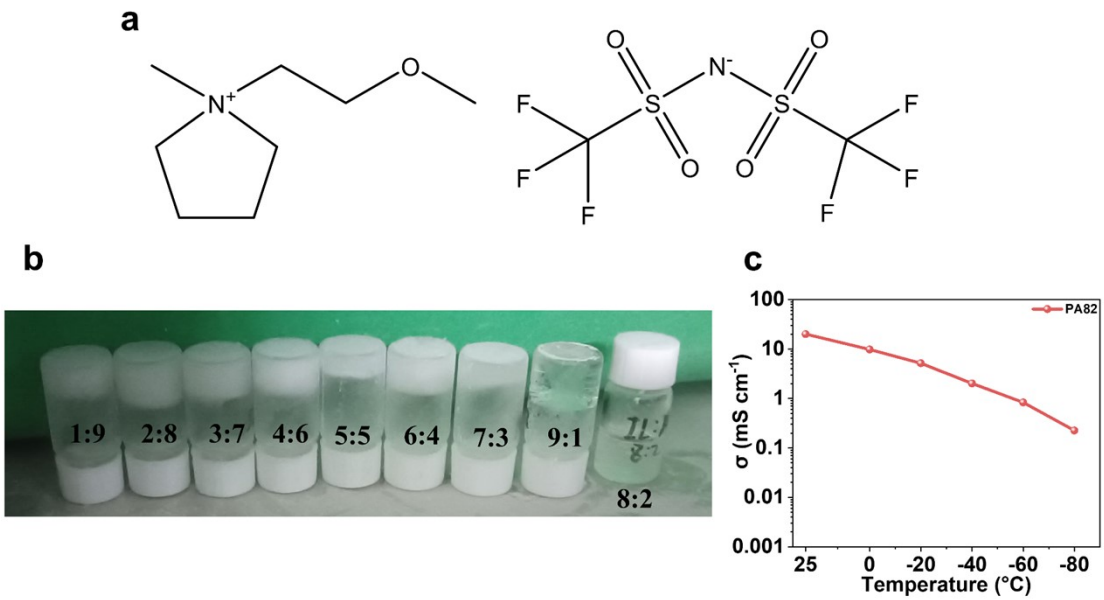

Fig. S1 (a) Structural formula of the ionic liquid $P_{1,2O1}$TFSI. (b) Optical images of $P_{1,2O1}$TFSI with different mass ratios of ACN at −85 °C. (c) Ionic conductivity of $P_{1,2O1}$TFSI with ACN at a mass ratio of 8:2. It was observed that at −85 °C, only the electrolyte at a mass ratio of 8:2 remained liquid, but showed a low ionic conductivity of 0.22 mS cm^{-1} at −80 °C.

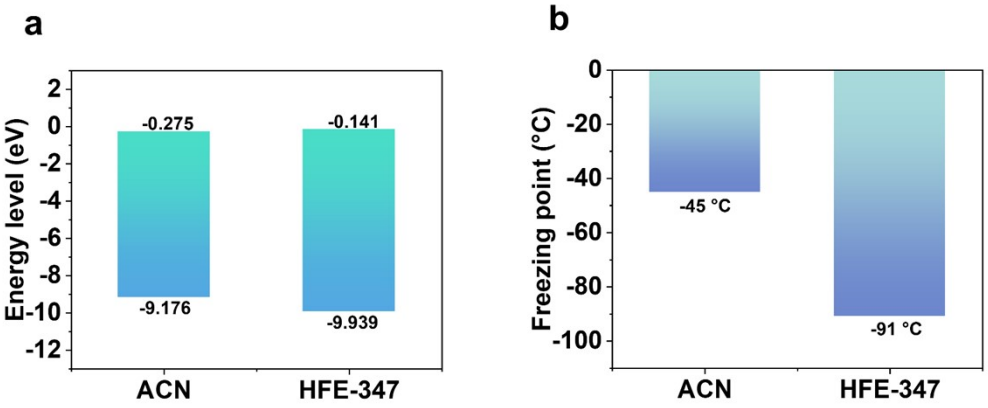

Fig. S2 (a) HOMO and LUMO energy levels of ACN and HFE-347. (b) Freezing points of ACN and HFE-347.

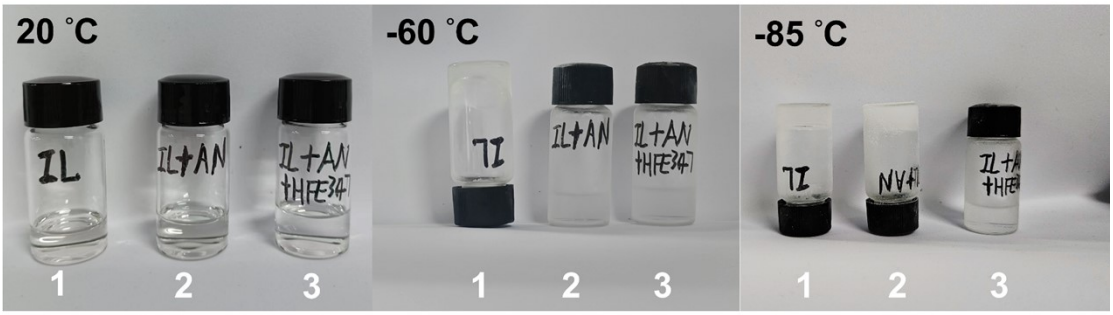

Fig. S3 Optical images of $P_{1,2O1}$TFSI (1), PA-1 (2) and PAH (3) electrolytes at temperatures of 20 °C (left), −60 °C (middle) and −85 °C (right). Only the PAH electrolyte remains unfrozen at −85 °C, demonstrating the role of the diluent HFE-347 in lowering the freezing point of the electrolyte.

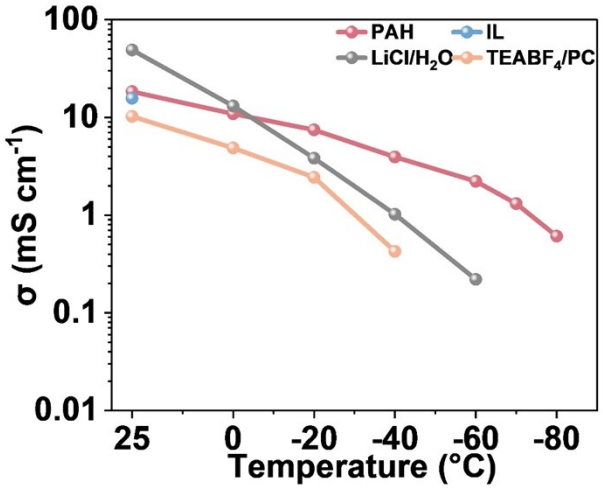

Fig. S4 Ionic conductivity of the PHA, $EMIMBF_4$ IL, aqueous 1M $LiCl/H_2O$, and 1M $TEABF_4$/PC organic electrolytes at different temperature.

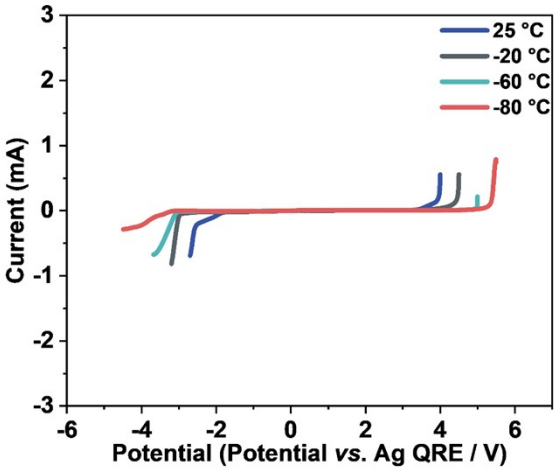

Fig. S5 LSV curves of the PAH electrolyte obtained from 25 °C to −80 ˚C with a scan rate of 10 mV s^{-1}. It is noted that the ESW of the PAH electrolyte gradually increased as the temperature decreased from 5.1 V at 25 °C and 6.6 V at −20 °C to 7.6 V at −60 °C and 8.1 V at −80 °C.

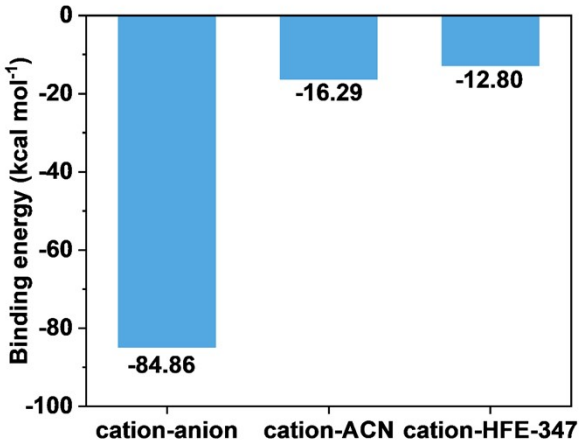

Fig. S6 Binding energies of cation-anion ($P_{1,201}^{+}$-TFSI⁻), cation-ACN and cation-HFE-347 obtained by DFT.

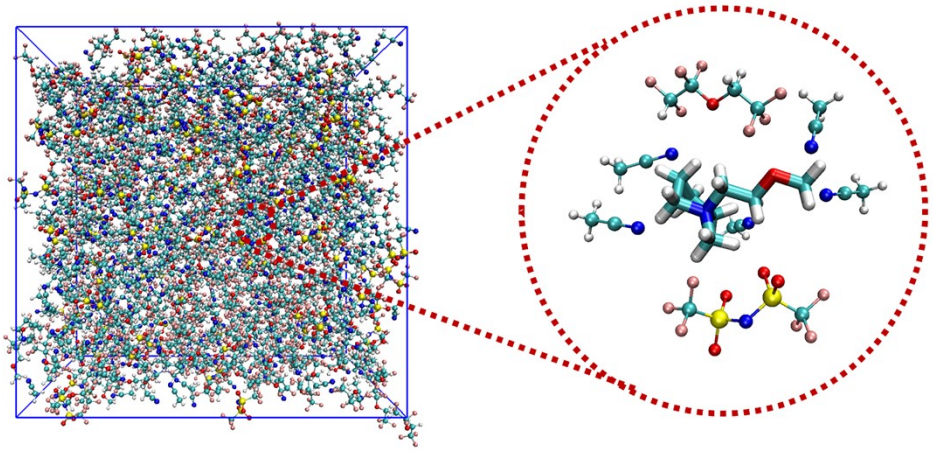

Fig. S7 Snapshot of the PAH electrolyte at 25 °C.

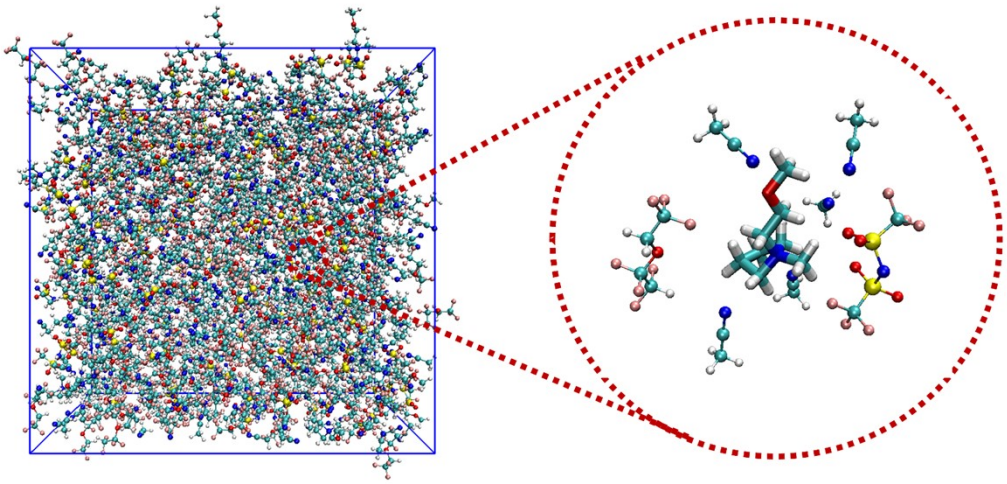

Fig. S8 Snapshot of the PAH electrolyte at −80 °C.

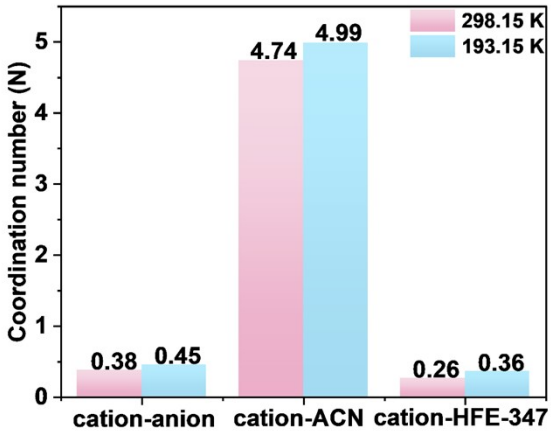

Fig. S9 Coordination numbers of the cation in the PAH electrolyte at 25 °C and −80 °C.

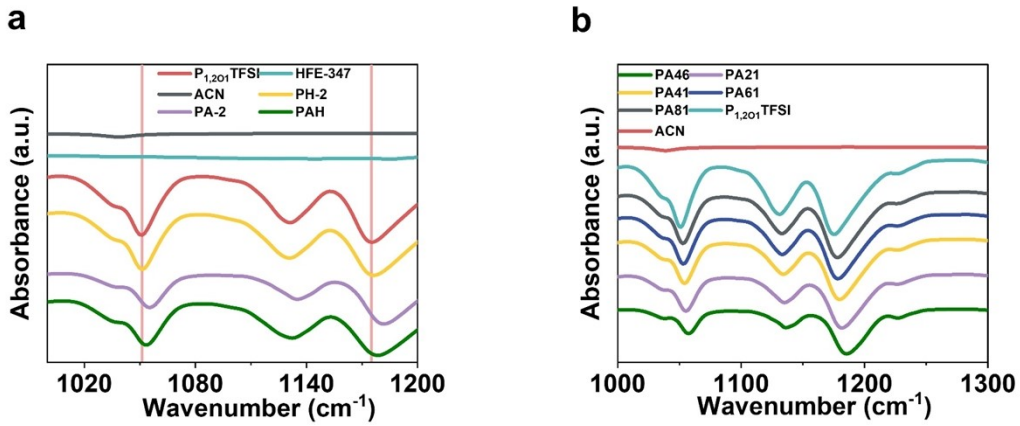

Fig. S10 FTIR-ATR spectra of the electrolytes and solvents at room temperature. (a) FTIR-ATR spectra of $P_{1,2O1}$TFSI, ACN, HFE-347, the PH-2, PA-2 and PAH electrolytes at room temperature. (b) FTIR-ATR spectra of ACN, $P_{1,2O1}$TFSI and their mixtures in different proportions at 25 °C (mass ratio). The PA-2 electrolyte is a mixture of $P_{1,2O1}$TFSI and ACN at a mass ratio of 2:1, while the PH-2 electrolyte is a mixture of $P_{1,2O1}$TFSI and HFE-347 at a mass ratio 1:1 (to be consistent with the component ratios of the PAH electrolyte).

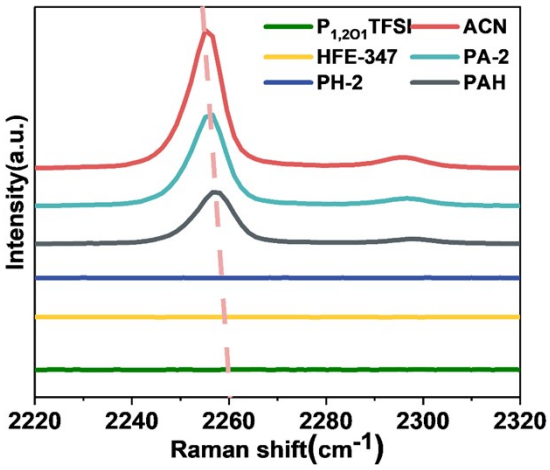

Fig. S11 Raman spectra of $P_{1,2O1}$TFSI, ACN, HFE-347, and the PH-2, PA-2 and PAH electrolytes at room temperature.

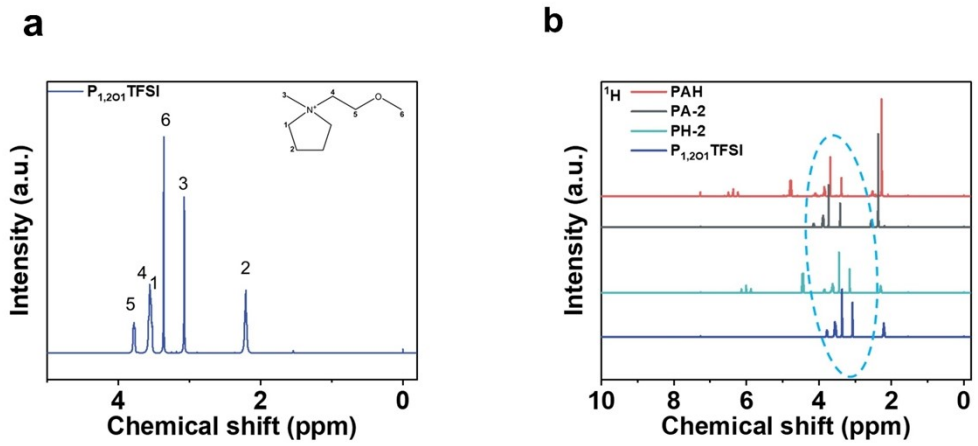

Fig. S12 ^{1}H NMR chemical shift of the different electrolytes at 25 °C. (a) ^{1}H NMR chemical shift of the $P_{1,2O1}$TFSI. (b) Difference between the ^{1}H NMR chemical shifts of $P_{1,2O1}$TFSI, the PH-2, PA-2 and PAH electrolytes. For room temperature NMR tests, deuterated chloroform was used as the deuterium solvent, with tetramethylsilane as the internal standard.

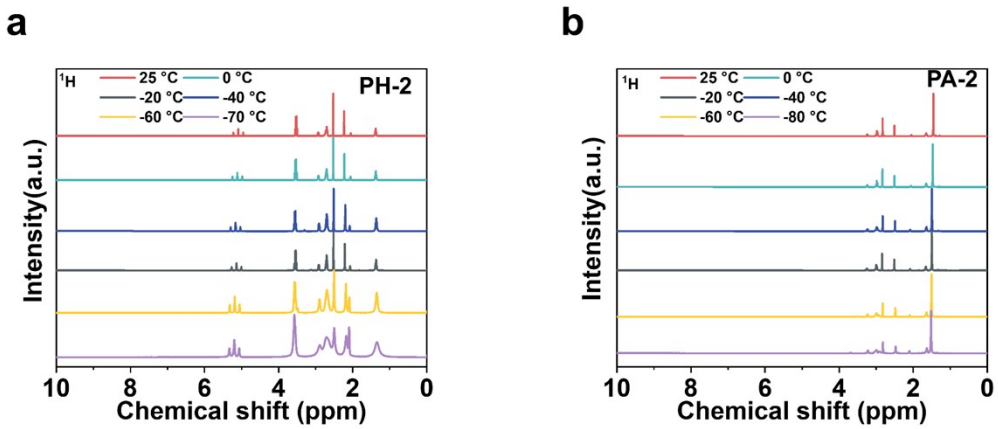

Fig. S13 ^{1}H NMR chemical shift differences of the PH-2 and PA-2 electrolytes from 25 °C to −80 °C. (a) The PH-2 electrolyte and (b)The PA-2 electrolyte. For the low-temperature NMR tests, deuterated chloroform was replaced by deuterated acetone. At exceptionally low temperatures, the chemical shifts are changed, which is attributed to the increased viscosity of the electrolyte.

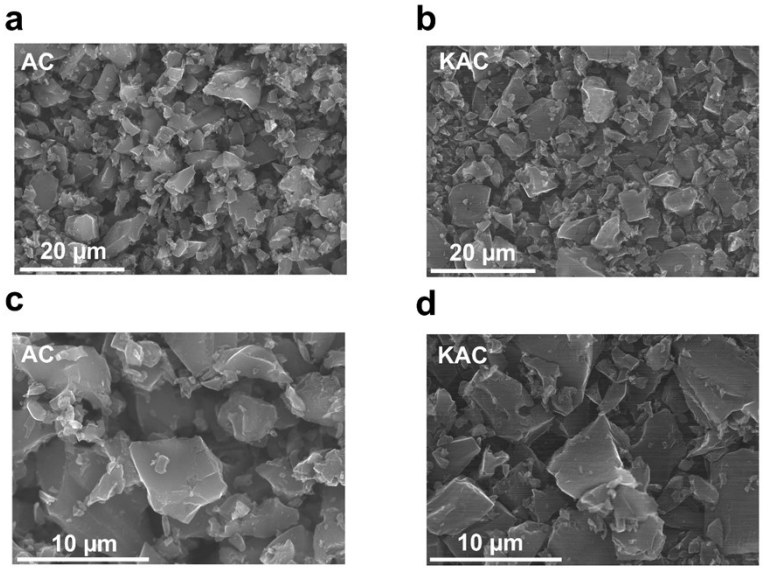

Fig. S14 Low-magnification SEM images of (a) AC and (b) KAC, and high-magnification SEM images of (c) AC and (d) KAC.

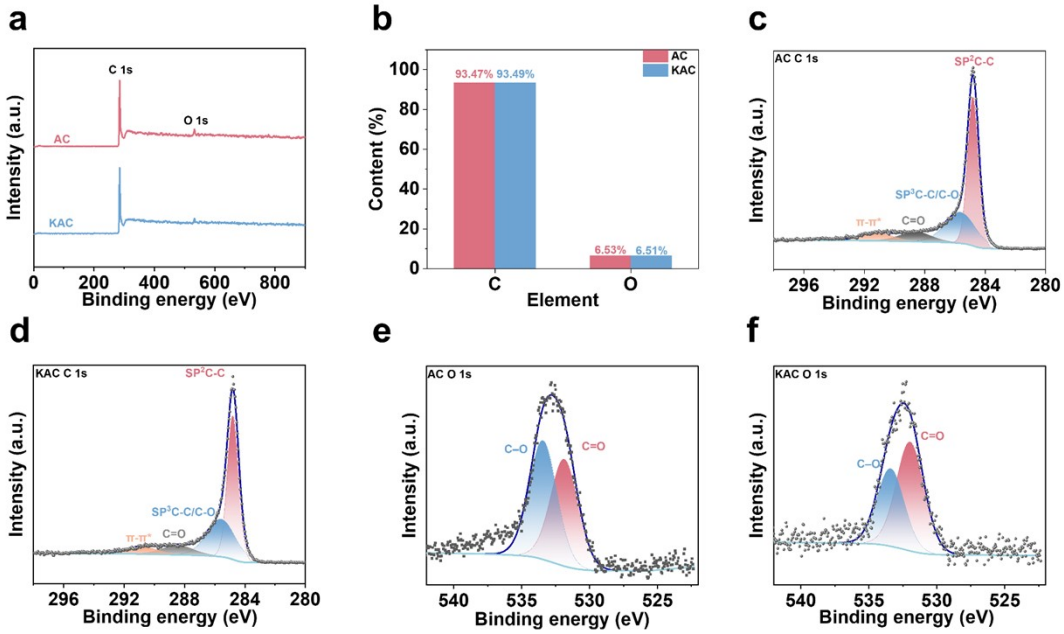

Fig. S15 (a) XPS survey spectra of AC and KAC. (b) Surface elemental composition (C and O) of AC and KAC. (c, d) C 1s XPS spectra of (c) AC and (d) KAC. (e, f) O 1s XPS spectra of (e) AC and (f) KAC.

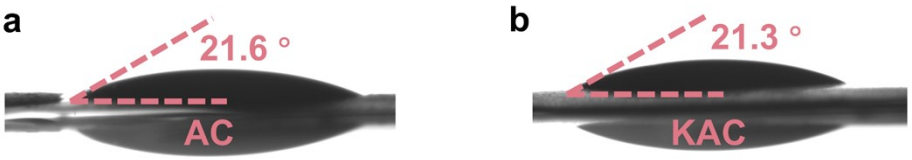

Fig. S16 Contact angles of (a) AC-based and (b) KAC-based electrodes.

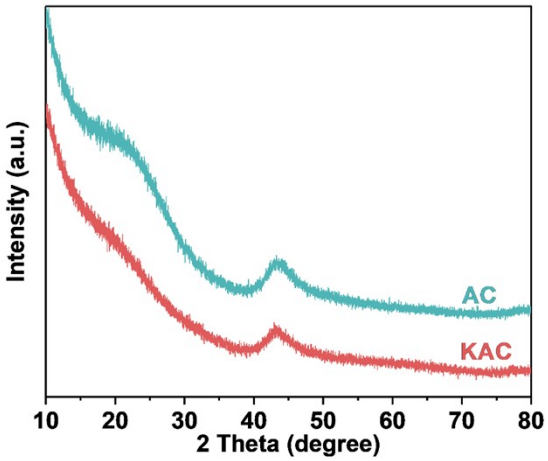

Fig. S17 XRD patterns of AC and KAC.

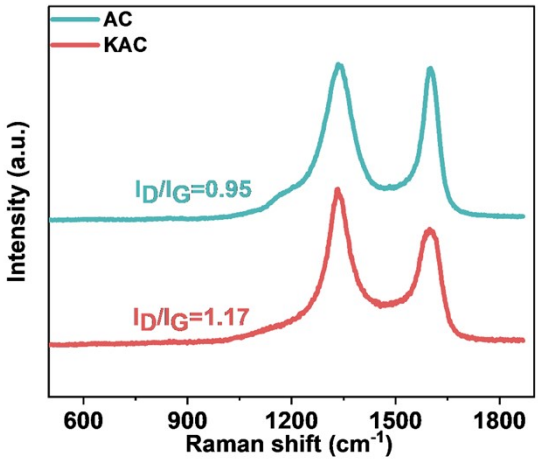

Fig. S18 Raman spectra of AC and KAC.

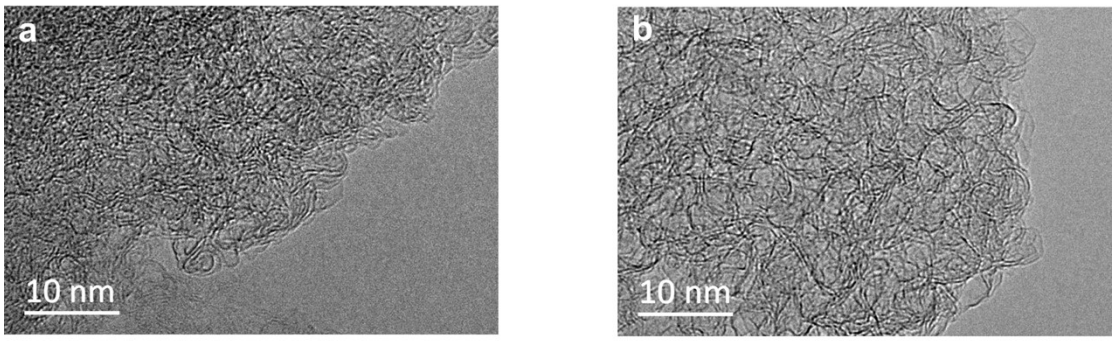

Fig. S19 HRTEM images of (a) AC and (b) KAC.

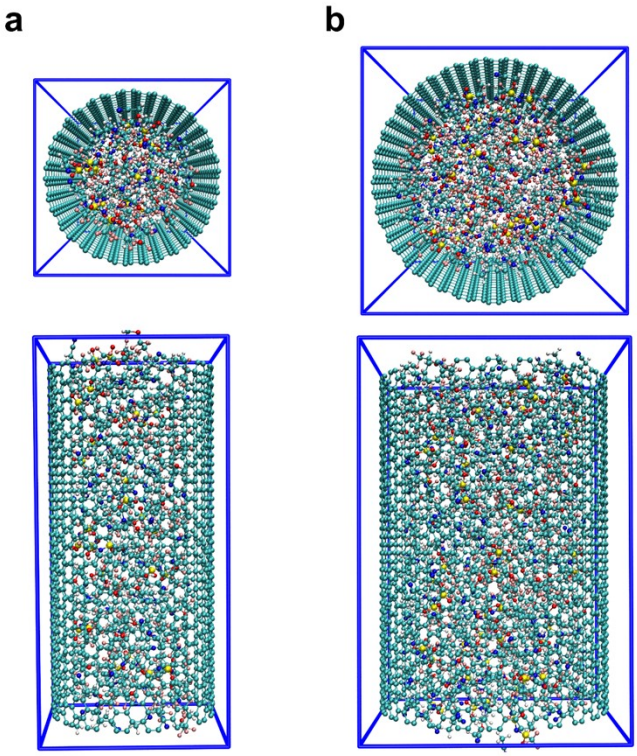

Fig. S20 Simulation of cation diffusion in PAH electrolytes within nanoporous models featuring distinct pore sizes**.** (a) 2.29 nm and (b) 3.36 nm.

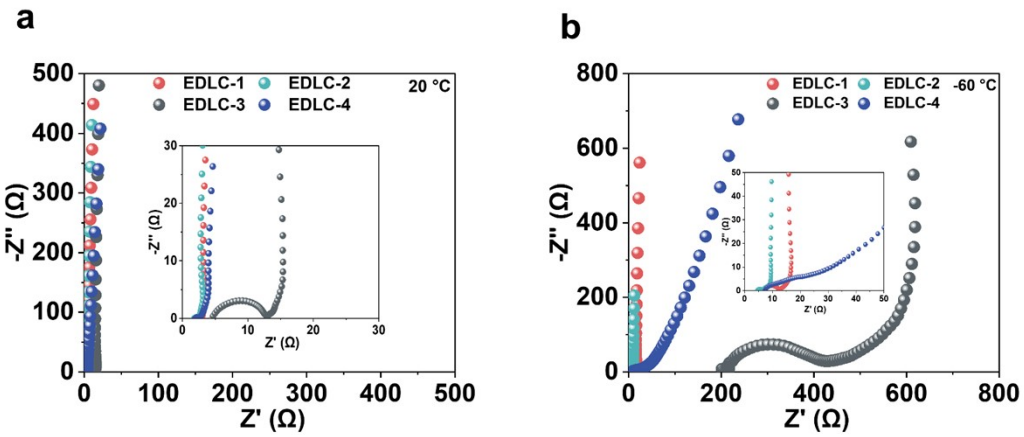

Fig. S21 EIS spectra of the four different EDLCs at (a) 20 °C and (b) −60 °C.

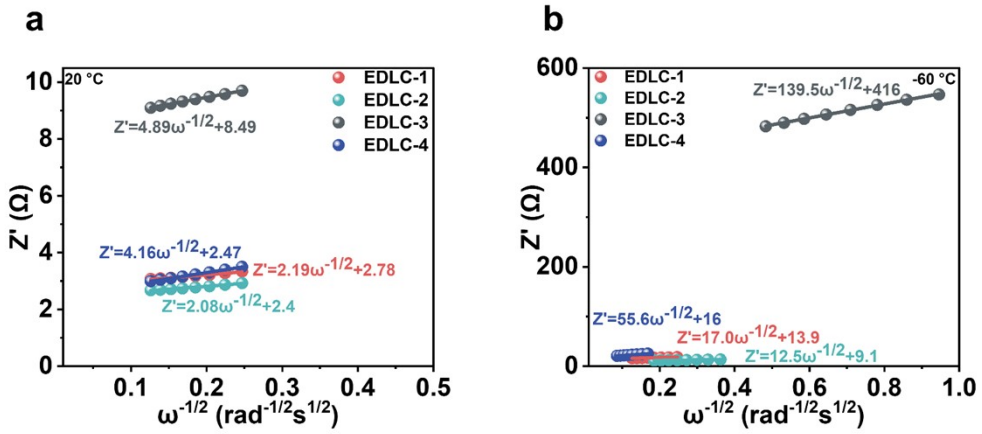

Fig. S22 Linear fitting of Z' versus $\omega^{-1/2}$ from the low-frequency region of EIS at (a) 20 °C and (b) −60 °C.

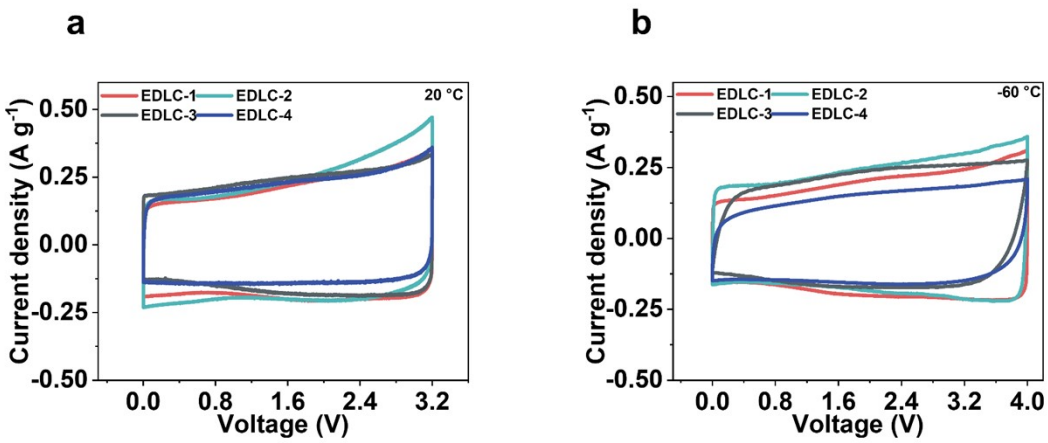

Fig. S23 CV curves of the four different EDLCs at (a) 20 °C and (b) −60 °C with a scan rate of 5 mV s^{-1}.

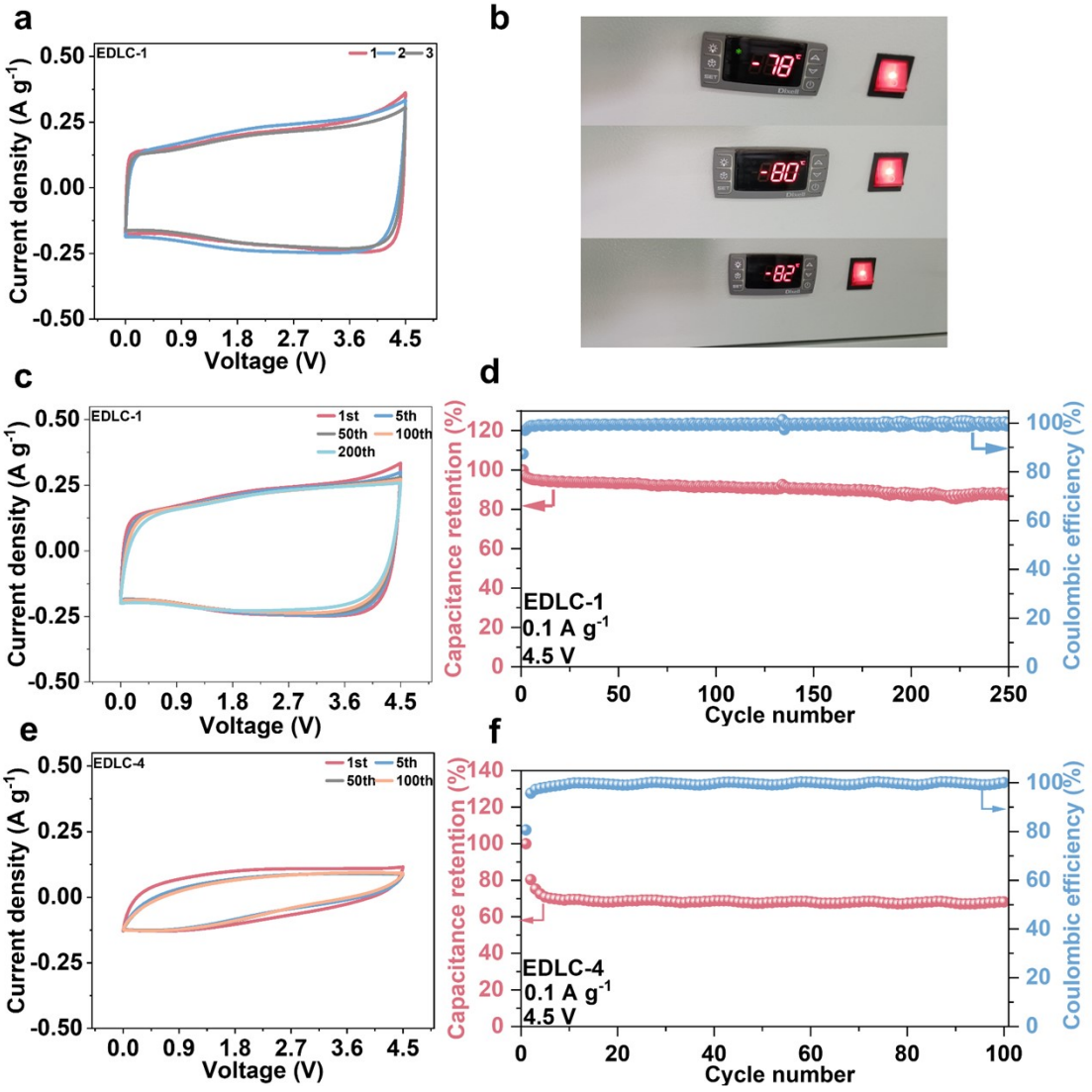

Fig. S24 (a) CV curves of three EDLC-1 devices measured at −80 °C and 5 mV s^{-1}. (b) Temperature fluctuations in the low-temperature chamber during the isothermal holding process. (c) CV curves of EDLC-1 at −80 °C and a scan rate of 5 mV s^{-1}. (d) Cycling performance of EDLC-1 at −80 °C and a low current density of 0.1 A g^{-1}. (e) CV curves of EDLC-4 at −80 °C and a scan rate of 5 mV s^{-1}. (f) Cycling performance of EDLC-4 at −80 °C and a low current density of 0.1 A g^{-1}. It is noted that slight variations can be observed among the three EDLC-1 devices, which are attributed to inherent device-

to-device variation and minor temperature fluctuations (Fig. S24b) in the low-temperature chamber.

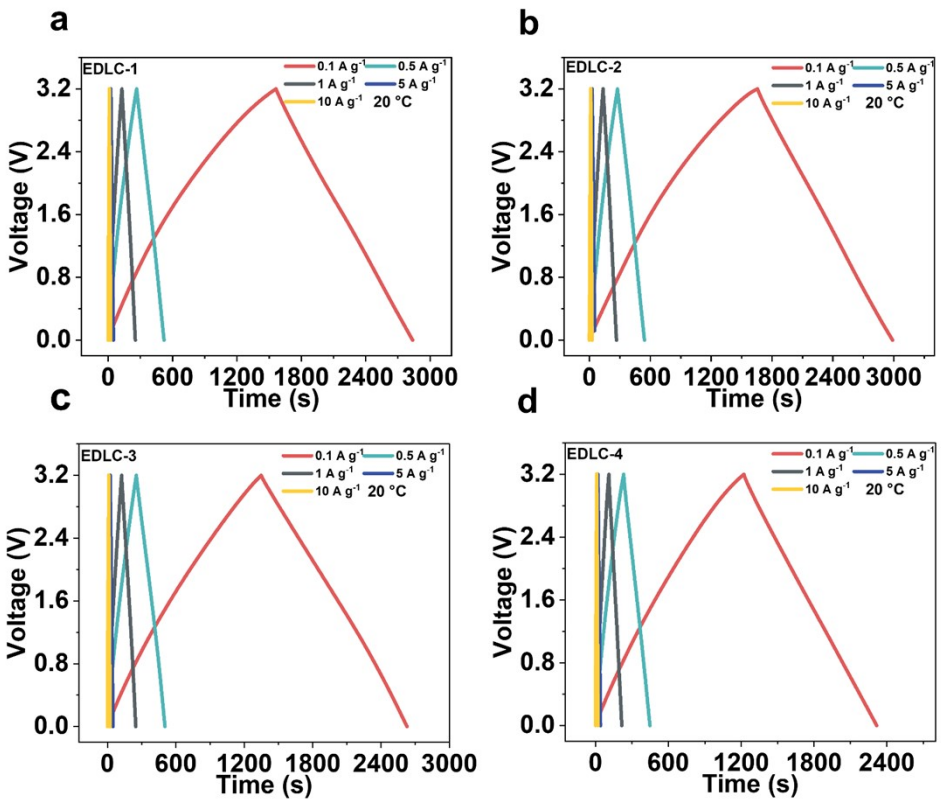

Fig. S25 GCD profiles of the four different EDLCs at 20 °C and current densities ranging from 0.1 A g^{-1} to 10 A g^{-1}. (a) EDLC-1. (b) EDLC-2. (c) EDLC-3. (d) EDLC-4.

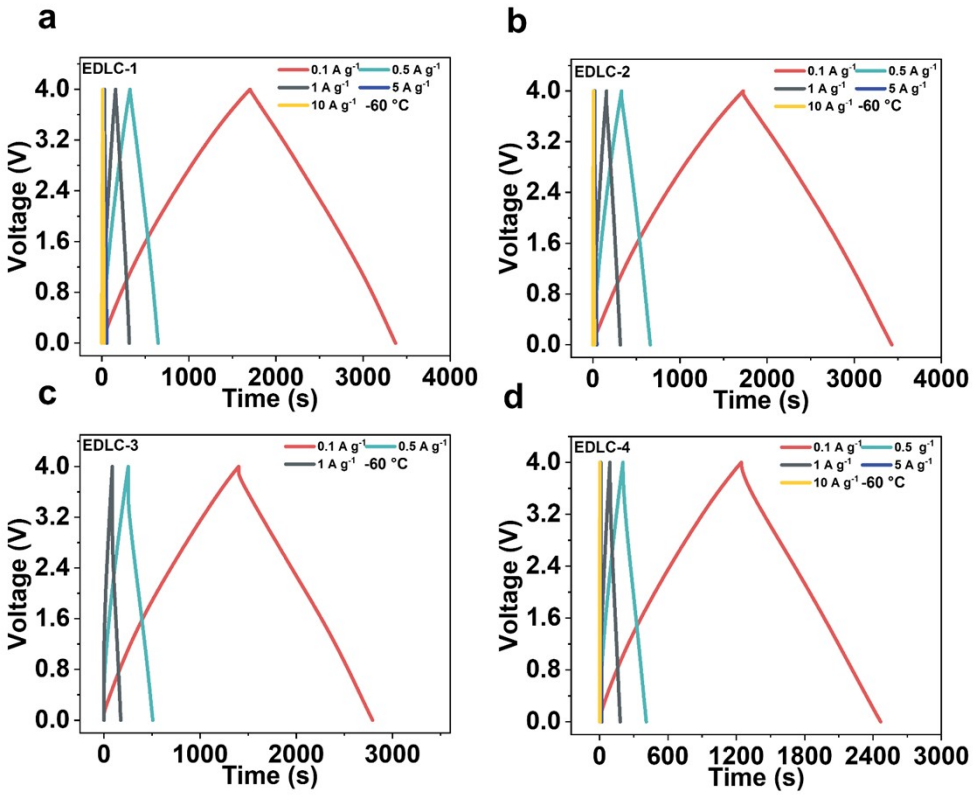

Fig. S26 GCD profiles of the four different EDLCs at −60 °C and current densities ranging from 0.1 A g^{-1} to 10 A g^{-1}. (a) EDLC-1. (b) EDLC-2. (c) EDLC-3. (d) EDLC-4. It is noted that EDLC-3 can't be operated at current densities exceeding 1 A g^{-1}.

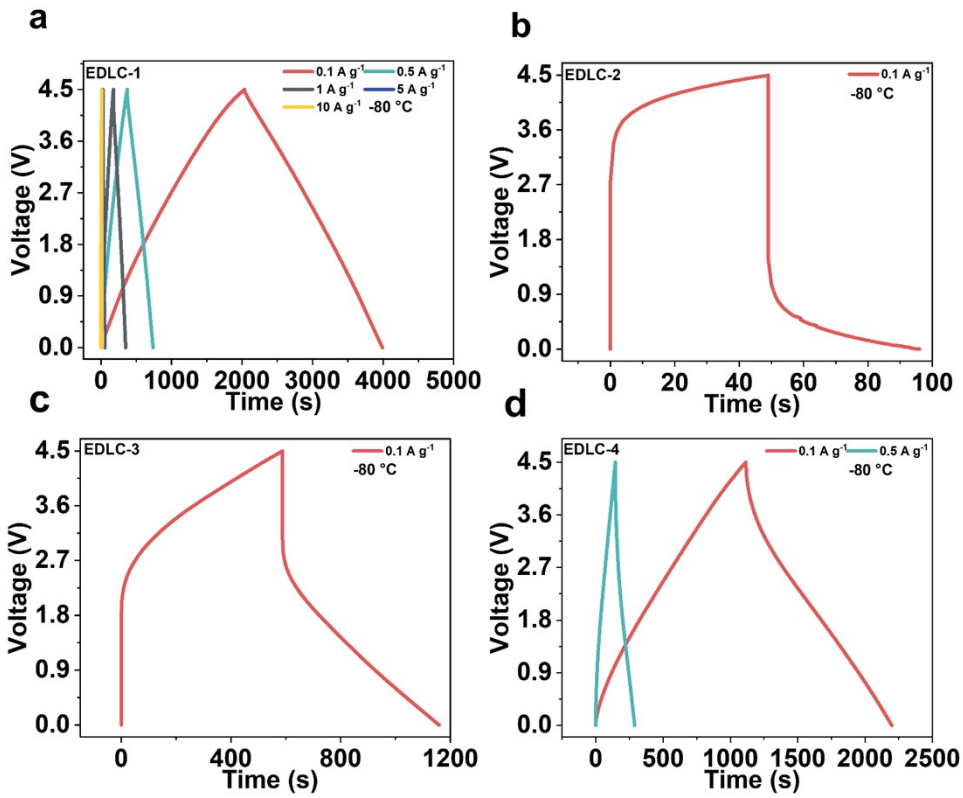

Fig. S27 GCD profiles of the four different EDLCs at −80 °C and current densities ranging from 0.1 A g^{-1} to 10 A g^{-1}. (a) EDLC-1. (b) EDLC-2. (c) EDLC-3. (d) EDLC-4. It is noted that EDLC-2, EDLC-3, and EDLC-4 were unable to operate at high current densities, indicating their instability under these conditions.

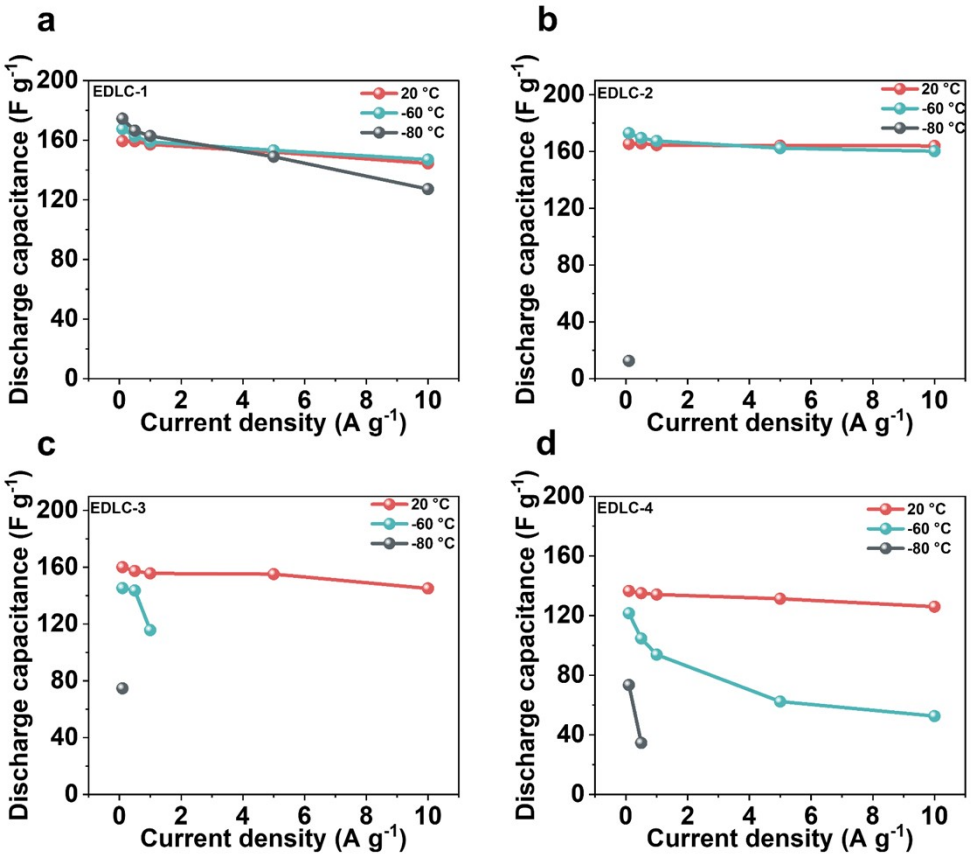

Fig. S28 Specific capacitance of the four different EDLCs at different temperatures and different current densities. (a) EDLC-1. (b) EDLC-2. (c) EDLC-3. (d) EDLC-4. It is noted that EDLC-2, EDLC-3, and EDLC-4 were unable to operate at −80 °C and at high current densities.

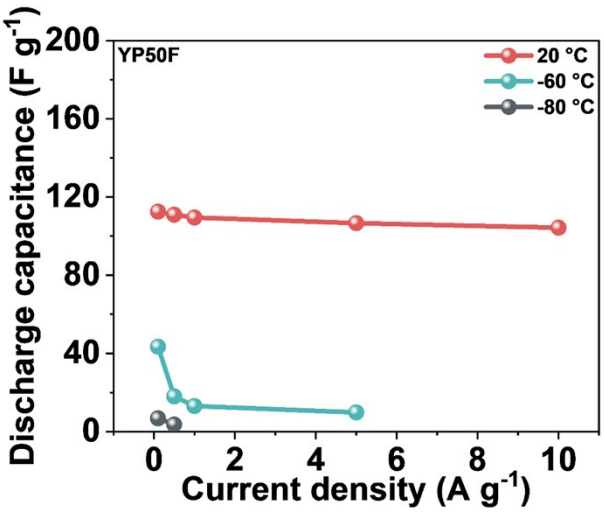

Fig. S29 Specific capacitance of the YP50F-based EDLCs at different temperatures and different current densities. It is noted that YP50F-based EDLCs were unable to operate at −80 °C and at high current densities.

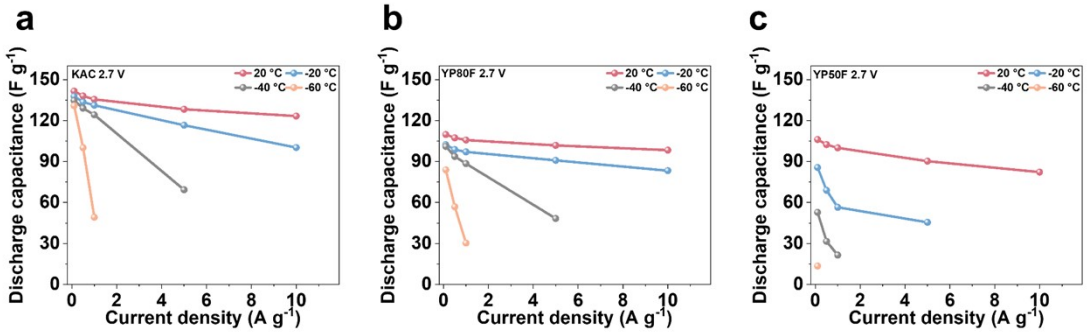

Fig. S30 Discharge capacitance of the EDLCs at different temperatures and different current densities based on KAC, YP80F, and YP50F with the commercial electrolyte 1M $TEABF_4$/PC.

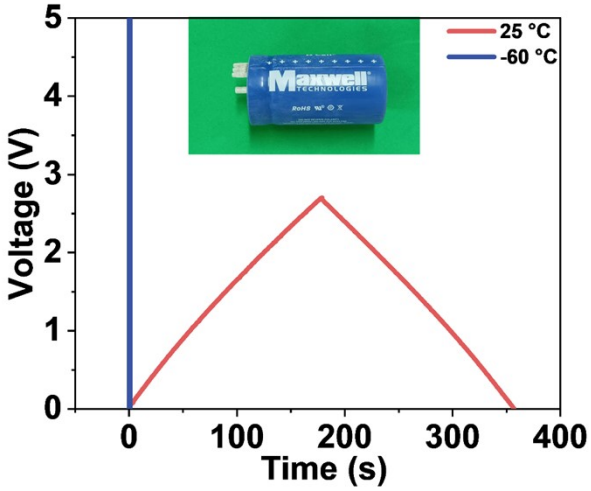

Fig. S31 GCD profiles of a commercial EDLC (Maxwell, 2.7 V, 310 F) at different temperatures and a current of 5 A. It is noted that the commercial EDLC failed to operate at −60 °C.

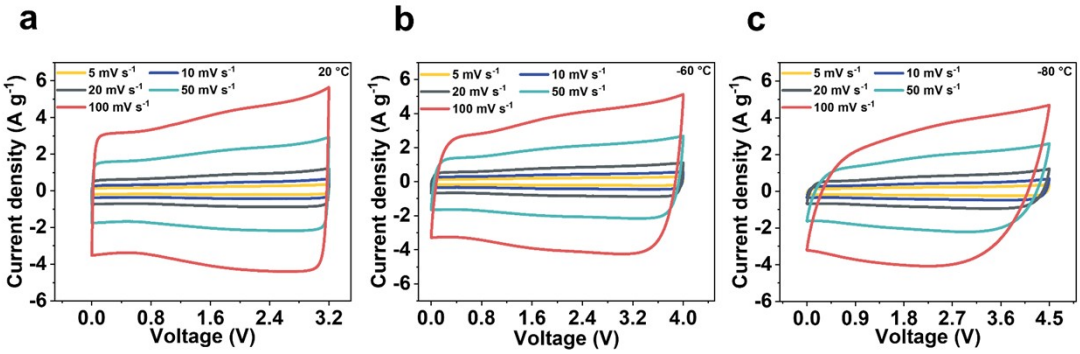

Fig. S32 CV curves of EDLC-1 with different scan rates at (a) 20 °C, (b) −60 °C and (c) −80 °C.

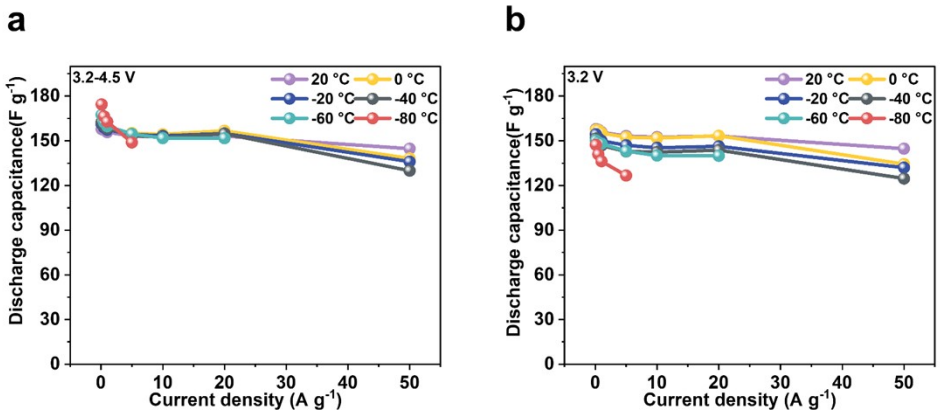

Fig. S33 Discharge capacitance of EDLC-1 at different temperatures and different current densities. (a) Discharge capacitance as a function of current density at 3.2 V (20 °C) to 4.5 V (−80 °C). (b) Discharge capacitance as a function of current density at 3.2 V ranging from 20 to −80 °C.

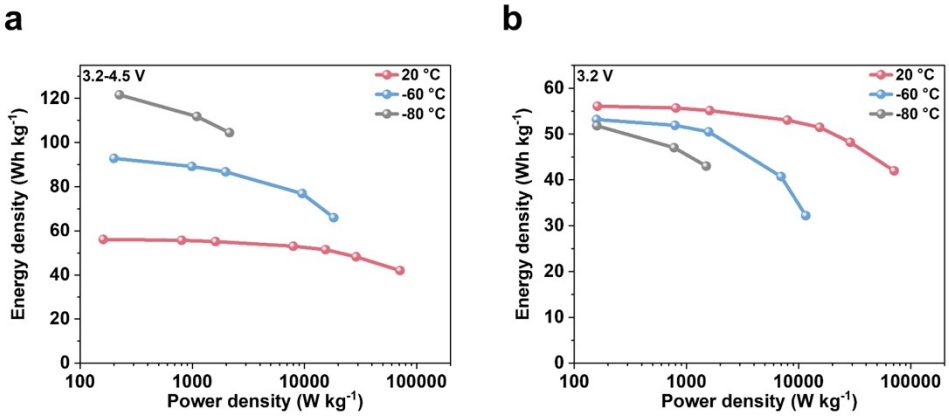

Fig. S34 Ragone plot of EDLC-1 at different temperatures and different current densities. (a) Energy density and power density at 3.2 V (20 °C) to 4.5 V (−80 °C). (b) Energy density and power density at 3.2 V (20 to −80 °C).

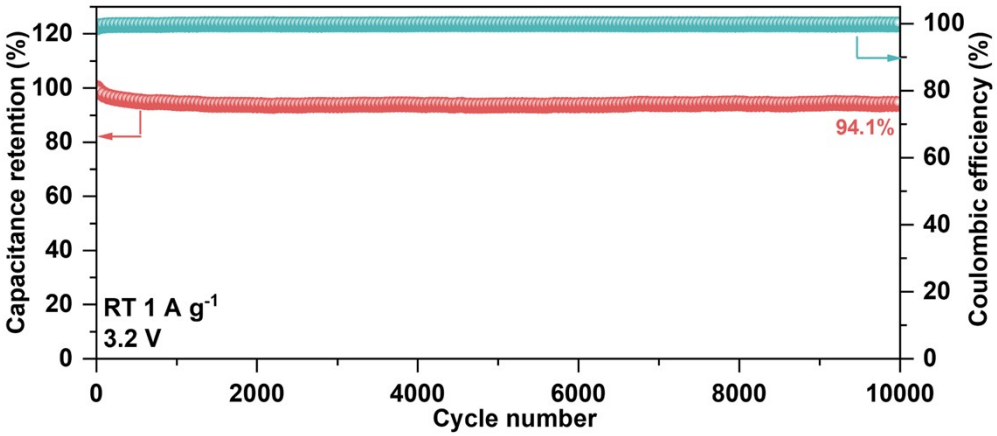

Fig. S35 Cycling performance of EDLC-1 (3.2 V) at room temperature and a current density of 1 A g^{-1}.

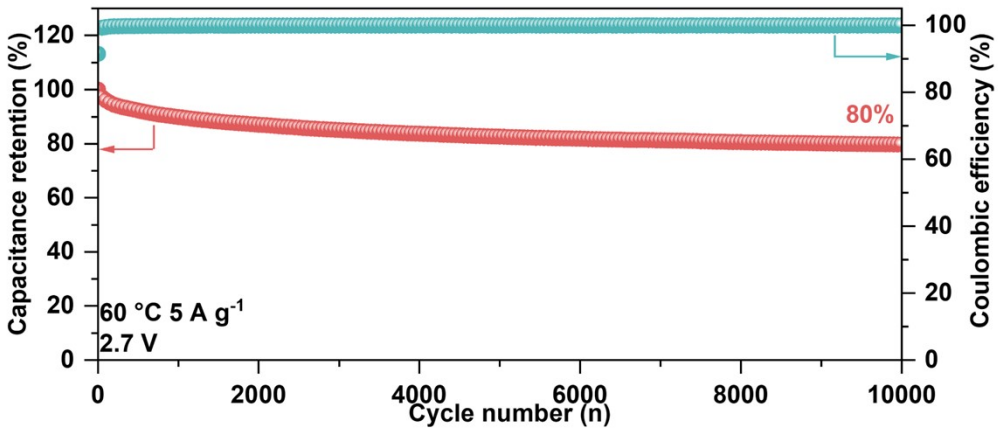

Fig. S36 Cycling performance of EDLC-1 (2.7 V) at 60 °C and a current density of 5 A g^{-1}.

Fig. S37 42 LED lights powered by EDLC-1 (CR2016 coin-type) at −80 °C.

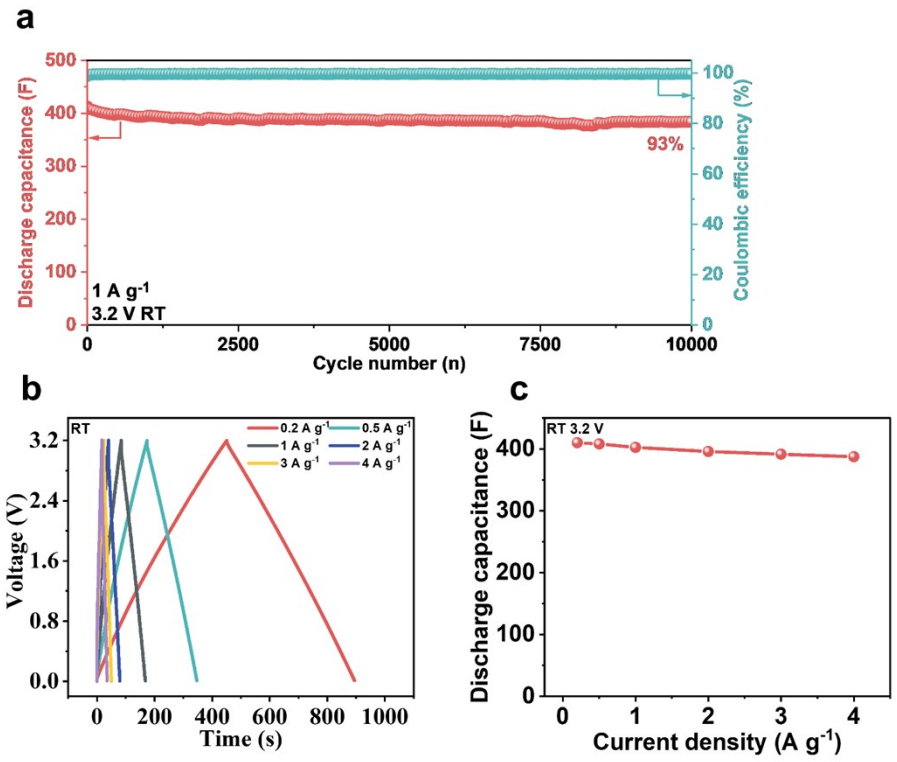

Fig. S38 Electrochemical performance of a pouch-type EDLC-1 (>300 F) test at 25 °C. (a) Cycling performance. (b) GCD profiles tested at different current densities. (c) Discharge capacitance as a function of different current densities.

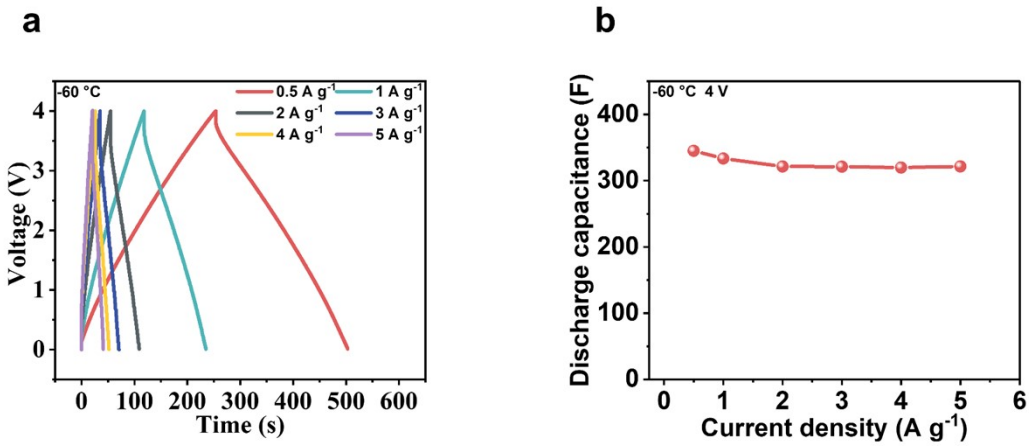

Fig. S39 Electrochemical performance of a pouch-type EDLC-1 (>300 F) test at −60 °C.

(a) GCD profiles. (b) Discharge capacitance as a function of different current densities.

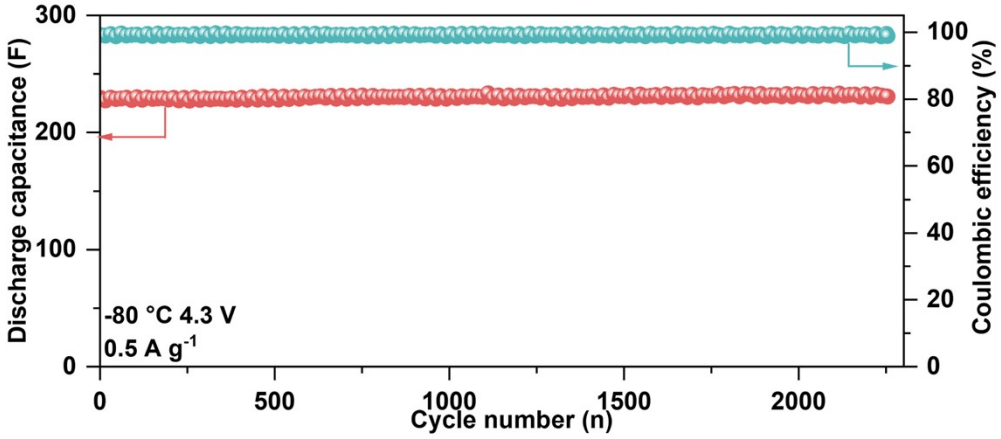

Fig. S40 Cycling performance of a pouch-type EDLC-1 tested at −80 °C.

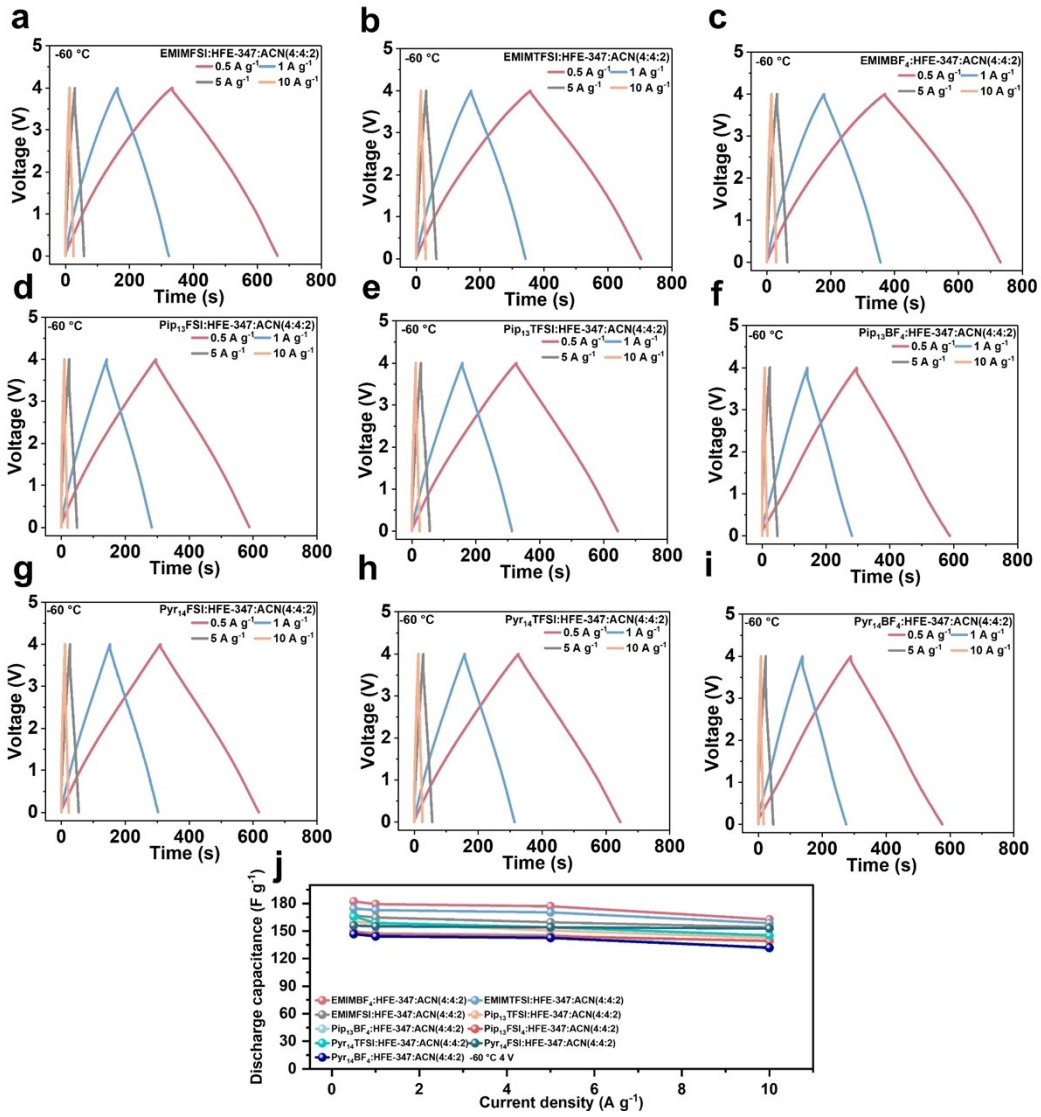

Fig. S41 GCD profiles and discharge capacitance of the PAH electrolyte-based EDLCs replacing $P_{1,2O1}TFSI$ with other ionic liquids at −60 °C. GCD profiles of the PAH electrolyte obtained by replacing $P_{1,2O1}TFSI$ by (a) ionic liquid 1-ethyl-3-methylimidazolium bis(fluorosulfonyl)imide (EMIMFSI), (b) ionic liquid 1-ethyl-3-methylimidazolium bis(trifluoromethanesulfonyl)imide (EMIMTFSI), (c) ionic liquid 1-ethyl-3-methylimidazolium tetrafluoroborate ($EMIMBF_4$), (d) ionic liquid N-methyl-N-propylpiperidinium bis(fluorosulfonyl)imide ($Pip_{13}FSI$), (e) ionic liquid N-methyl-N-propylpiperidinium bis(trifluoromethanesulfonyl)imide ($Pip_{13}TFSI$), (f) ionic liquid N-methyl-N-propylpiperidinium tetrafluoroborate ($Pip_{13}BF_4$), (g) ionic liquid N-methyl-N-

butylpyrrolidinium bis(fluorosulfonyl)imide ($Pip_{13}FSI$), (h) ionic liquid N-methyl-N-butylpyrrolidinium bis(trifluoromethanesulfonyl)imide ($Pip_{13}TFSI$) and (i) ionic liquid N-methyl-N-butylpyrrolidinium tetrafluoroborate ($Pip_{13}BF_4$). (j) Discharge capacitance as a function of different current densities of the EDLCs based on the PHA electrolytes by replacing $P_{1,2O1}TFSI$ with other ionic liquids, tested at −60 °C.

Table S1 Specific surface area and pore-size summary of AC and KAC from nitrogen adsorption-desorption isotherm analysis.

Sample	Specific surface area ($m^2 g^{-1}$)	Total pore volume ($cm^3 g^{-1}$)	Micropore volume ($cm^3 g^{-1}$)	Average pore diameter (nm)
AC	2121	1.21	0.23	2.29
KAC	3240	2.71	0.21	3.36

Table S2 Calculated diffusion coefficients of the four different EDLCs at different temperatures by EIS.

Sample	Diffusion coefficient (20 °C, $cm^2 s^{-1}$)	Diffusion coefficient (−60 °C, $cm^2 s^{-1}$)	Diffusion coefficient (−80 °C, $cm^2 s^{-1}$)
EDLC-1	4.3×10^{-9}	3.54×10^{-11}	5.38×10^{-12}
EDLC-2	7.43×10^{-9}	1.09×10^{-10}	1.99×10^{-14}
EDLC-3	5.73×10^{-10}	3.72×10^{-13}	8.58×10^{-14}
EDLC-4	1.12×10^{-9}	3.3×10^{-12}	1.42×10^{-13}

Table S3 Comparison of electrochemical performance of EDLC-1 with other reported EDLCs.

Electrolyte	Electrode material	Voltage	T_{min}	C_E	E_{max}	Refs.
$PMImNTf_2$, ACN, and MB (volume ratio of 1:1:1)	Activated carbon	2.8 V	−70 °C	30 F g^{-1} (0.5 A g^{-1} −70 °C)	5.9 Wh kg^{-1} (2.8 kW kg^{-1} −60 °C)	1
0.5 M TEMA-BF_4 in ACN and ACT (volume ratio of 1:1)	Activated carbon	2.7 V	−70 °C	83.6 F g^{-1} (20 mV s^{-1} −70 °C)	11.79 Wh kg^{-1} (6.8 kW kg^{-1} −70 °C)	14
[EMIm][FSI], [EMIm][BF_4], and [EMIm][TCB] (molar ratio of 6:1:3)	SiO_2-templated carbon	3.2 V	−50 °C	91 F g^{-1} (0.2 A g^{-1} −50 °C)	5.2 Wh kg^{-1} (1000 W kg^{-1} −50 °C)	15
3.8 m $CaCl_2$ in H_2O	Activated carbon	1.8 V	−50 °C	186.4 F g^{-1} (1 A g^{-1} −50 °C)	-	16
LiTFSI, DMSO and H_2O (mass ratio of 65.45:23.65:10.90)	Porous carbon	2.6 V	–35 °C	89 F g^{-1} (1A g^{-1} −35 °C)	30 Wh kg^{-1} (300 W kg^{-1} −35 °C)	17
5 M LiTFSI in ACN and H_2O (molar ratio of 1.156:1.111)	Activated carbon	2.2 V	−30 °C	34.4 F g^{-1} (10 A g^{-1} −30 °C)	-	18

$Pip_{13}FSI$ and $Pyr_{14}FSI$ (molar ratio of 1:1)	Graphene oxide	3 V	−50 °C	100~120 F g^{-1} (1 mV s^{-1} −40 °C)	-	19
0.5 M $MeEt_3NBF_4$ in ACN and DIOX (volume ratio of 3:7)	Activated carbon	2.5 V	−100 °C	164 F g^{-1} (5 mV s^{-1} −100 °C)	-	20
3.5 m $Mg(ClO_4)_2$	Porous carbon	1.8~2.4 V	−60 °C	212 F g^{-1} (1 A g^{-1} −60 °C)	42.5 Wh kg^{-1} (600 W kg^{-1} −60 °C)	21
4.2 m $Ca(ClO_4)_2$ in H_2O and ACN (mass ratio of 10:9)	Porous carbon	2.3~2.8 V	−50 °C	212 F g^{-1} (1 A g^{-1} −50 °C)	50.6 Wh kg^{-1} (700 W kg^{-1} −50 °C)	22
1.1 M $DMPBF_4$ in DMF and ACT (volume ratio of 2:8)	Activated carbon	2.7 V	−70 °C	100 F g^{-1} (20 mV s^{-1} −70 °C)	25.08 Wh kg^{-1} (667 W kg^{-1} −70 °C)	23
10 m CsAc in H_2O	Activated carbon	1.2 V	-95 °C	200 mF cm^{-2} (0.1 mA cm^{-2} −95 °C)	-	24
$P_{1,2O1}TFSI$, HFE-347 and ACN (mass ratio of 4:4:2)	KOH-etched YP80F	3.2~4.5 V	−80 °C	162.8 F g^{-1} (1 A g^{-1} −80 °C 4.5 V) 136.3 F g^{-1} (1 A g^{-1} −80 °C 3.2 V)	104.5 Wh kg^{-1} (2149 W kg^{-1} −80 °C 4.5 V) 43 Wh kg^{-1} (1503 W kg^{-1} −80 °C 3.2 V)	This work

Supplementary references

1. X. Tang, D. Xiao, Z. Xu, Q. Liu, B. Ding, H. Dou and X. Zhang, *J. Mater. Chem. A*, 2022, **10**, 18374–18382.
2. Y. Song, T. Liu, M. Li, B. Yao, T. Kou, D. Feng, F. Wang, Y. Tong, X.-X. Liu and Y. Li, *Adv. Energy Mater.*, 2018, **8**, 1801784.
3. W. J. Hehre, R. Ditchfield and J. A. Pople, *J. Chem. Phys.*, 1972, **56**, 2257–2261.
4. A. D. Becke, *J. Chem. Phys.*, 1993, **98**, 5648–5652.
5. Grimme, S. Ehrlich and L. Goerigk, *J. Comput. Chem.*, 2011, **32**, 1456–1465.
6. S. Grimme, J. Antony, S. Ehrlich and H. Krieg, *J. Chem. Phys.*, 2010, **132**, 154104.
7. T. Lu and F. Chen, *J. Comput. Chem.*, 2012, **33**, 580–592.
8. W. Humphrey, A. Dalke and K. Schulten, *J. Mol. Graph.*, 1996, **14**, 33–38.
9. N. Schmid, A. P. Eichenberger, A. Choutko, S. Riniker, M. Winger, A. E. Mark and W. F. van Gunsteren, *Eur. Biophys. J.*, 2011, **40**, 843–856.
10. M. J. Abraham, T. Murtola, R. Schulz, S. Páll, J. C. Smith, B. Hess and E. Lindahl, *SoftwareX*, 2015, **1–2**, 19–25.
11. U. Essmann, L. Perera, M. L. Berkowitz, T. Darden, H. Lee and L. G. Pedersen, *J. Chem. Phys.*, 1995, **103**, 8577–8593.
12. B. Hess, *J. Chem. Theory Comput.*, 2008, **4**, 116–122.
13. H. Grubmüller, H. Heller, A. Windemuth and K. Schulten, *Mol. Simul.*, 1991, **6**, 121–142.
14. H. Yang, Z. Wang, Y. Qi, Q. Pan, C. Zhang, Y. Huang, J. Yan, K. Cen, G. Xiong, Z. Bo and K. (Ken) Ostrikov, *J. Mater. Chem. A*, 2023, **11**, 16995 – 17006.

15. E. P. Yambou, B. Gorska and F. Béguin, *ChemSusChem*, 2021, **14**, 1196–1208.
16. C. You, W. Wu, W. Yuan, P. Han, Q. Zhang, X. Chen, X. Yuan, L. Liu, J. Ye, L. Fu and Y. Wu, *Adv. Funct. Mater.*, 2023, **33**, 2208206.
17. X. Lu, R. J. Jiménez-Riobóo, D. Leech, M. C. Gutiérrez, M. L. Ferrer and F. del Monte, *ACS Appl. Mater. Interfaces*, 2020, **12**, 29181–29193.
18. Q. Dou, S. Lei, D.-W. Wang, Q. Zhang, D. Xiao, H. Guo, A. Wang, H. Yang, Y. Li, S. Shi and X. Yan, *Energy Environ. Sci.*, 2018, **11**, 3212–3219.
19. W.-Y. Tsai, R. Lin, S. Murali, L. Li Zhang, J. K. McDonough, R. S. Ruoff, P.-L. Taberna, Y. Gogotsi and P. Simon, *Nano Energy*, 2013, **2**, 403–411.
20. J. Xu, N. Yuan, J. M. Razal, Y. Zheng, X. Zhou, J. Ding, K. Cho, S. Ge, R. Zhang, Y. Gogotsi and R. H. Baughman, *Energy Storage Mater.*, 2019, **22**, 323–329.
21. Y. Liu, C. Yu, S. Lan, W. Liu and J. Qiu, *Adv. Funct. Mater*., 2025, **35**, 2421056.
22. Y. Liu, C. Yu, S. Lan, W. Liu and J. Qiu, *Adv. Mater*., 2025, **37**, 2503157.
23. Y. Qi, C. Bao, X. Li, J. Yan, K. Cen, Z. Bo and H. Yang, *Adv. Mater*., 2025, **37**, e09768.
24. M. Qiu, P. Sun, Y. Liang, J. Chen, Z. L. Wang and W. Mai, *Nat. Commun*., 2024, **15**, 10420.